Exciton-Polaron in a quasi-one-dimensional chain of hexyl-diammonium-BiI_5 octahedra

Dipin K. Tomar,[a*] Swapnil Deshpande,[b] Shubam Gupta,[c] Sudip Chakraborty,[b*] Pabitra K Nayak[c*] and Jyotishman Dasgupta[a*]

a. *Jyotishman Dasgupta & Dipin Kumar Tomar
Department of Chemical Sciences
Tata Institute of Fundamental Research, 1 Homi Bhabha Road, Mumbai 400005, India;
Email: dasgupta@tifr.res.in & dipin.tomar@tifr.res.in
b. *Sudip Chakraborty & Swapnil Deshpande
Materials Theory for Energy Scavenging (MATES) Lab,
Harish-Chandra Research Institute (HRI), A C.I. of Homi Bhabha National Institute (HBNI), Chhatnag Road, Jhunsi, Prayagraj, Allahabad 211019, India,
Email: sudipchakraborty@hri.res.in
c. *Pabitra Nayak & Shubham Gupta
Tata Institute of Fundamental Research, Go-panpally village, Sirilingampally, Hyderabad-500046, India;
Email: pabitra.nayak@tifrh.res.in

Abstract: Lower dimensional hybrid perovskite exhibits intriguing similarities to traditional quantum confined inorganic semiconductors with comparable exciton binding energies. The presence of flexible organic cations acting as spacers and stabilizers enhances electron-phonon couplings, further amplifying the potential for modular light-matter interactions in these materials. One-dimensional analogs of perovskite remain largely unexplored in the literature, representing a promising frontier for optoelectronic investigations. Herein we unravel the nature of excitons in a class of quasi-1D chain of corner-sharing Bismuth Iodide octahedral that mimics the low-dimensional hybrid organic-inorganic perovskite materials. Using broadband femtosecond impulsive Raman spectroscopy and detailed electronic structure calculations, we quantify the exciton lifetime and electron-phonon coupling constants to fully describe the excitation as an exciton-polaron. Our findings shed light on the immense potential of one-dimensional analogs of perovskites in developing novel materials with enhanced optoelectronic properties amenable to light conversion technologies.

Introduction

Photoinduced excitations within bulk semiconductors manifest as bound electron-hole quasiparticles capable of migrating through the material. These excitations, termed excitons, are formed immediately after light excitation, serving as the initial stage in light harvesting. The synthetic manipulation of these photogenerated excitons is pivotal for enhancing device performance. External perturbations, such as temperature variations affecting dynamics, electric fields inducing Stark shifts, and magnetic fields perturbing spin states, can be employed for exciton control. Intrinsic tuning of excitons is only achieved through rational material design for tailored functions. However, quantum confinement can provide a possible solution to adjust their stability and interactions, which is a promising development for optoelectronic devices such as LEDs, photodetectors, and spintronics[1]. A simple description of a confined system can be given from a two-particle Hamiltonian where the bound state solutions for the Hamiltonian have the expression-

$$E_{b,N} = \frac{R_y}{\left(N + \frac{\alpha - 3}{2}\right)^2}$$

Where α is the dimensionality of the system. As dimensionality is reduced, the bandgap of a material shifts to higher energies. This complexity has already been established in rigid 2-D, 1-D, and 0-D quantum wells such as transition metal dichalcogenides, carbon nanotubes, and quantum dots having characteristic large exciton binding, discrete energies, and strong photoluminescence[2]. The large exciton binding energies can drive important applications in quantum devices like monolayer FETs and single photon emitters as prominent examples[3,4].

Confinement enables multiple excitons to interact with each other or with free charges in the lattice, resulting in the formation of many body quasiparticles. For instance, in the case of two excitons interacting across two quantum wells, there are six accountable Coulomb interaction terms in the Hamiltonian[5]. For a bilayer quantum well, the model can be derived from a simple description of coulomb potentials,

$$v_{eh} = \frac{e_0^2}{\sqrt{r^2+d^2}},\ v_{ee} = v_{hh} = \frac{e_0^2}{r}$$

Where d is the separation between the quantum wells. As the distance increases between quantum wells, the dielectric and Coulomb screening of carriers reduces abruptly, making repulsion terms in the interacting Hamiltonian more significant. Such a change can be observed through pronounced red-shift of exciton resonances along with in some cases decreased oscillator strength and corresponding linewidth broadening due to carrier scattering. These changes can be observed and quantified by various pump-probe methods[6–8].

Although the excitonic parameters can be tuned by confinement, the synthesis of usual lower dimensional materials requires procedures such as stepwise exfoliation which may not be industrially scalable. Further, the formed structures are highly susceptible to oxygen and water. Organic-inorganic hybrid halide perovskites provide an advantage over traditional quantum wells and can simply be assembled to form quantum well like structures by solution processing, where excitation is confined to a few angstrom regimes. The design of organic-inorganic hybrid perovskites is a mere consequence of the packing of organic and inorganic moieties in the structure. The inorganic unit comprises metal halide octahedra MX_6 that can be connected in face-sharing, edge-sharing, and corner-sharing units. These connectivities result from the packing of surrounding organic cations that stabilize the inorganic octahedra. The size criteria for organic cation forming 3D

https://doi.org/10.26434/chemrxiv-2024-12c67 **ORCID:** https://orcid.org/0000-0003-4607-653X

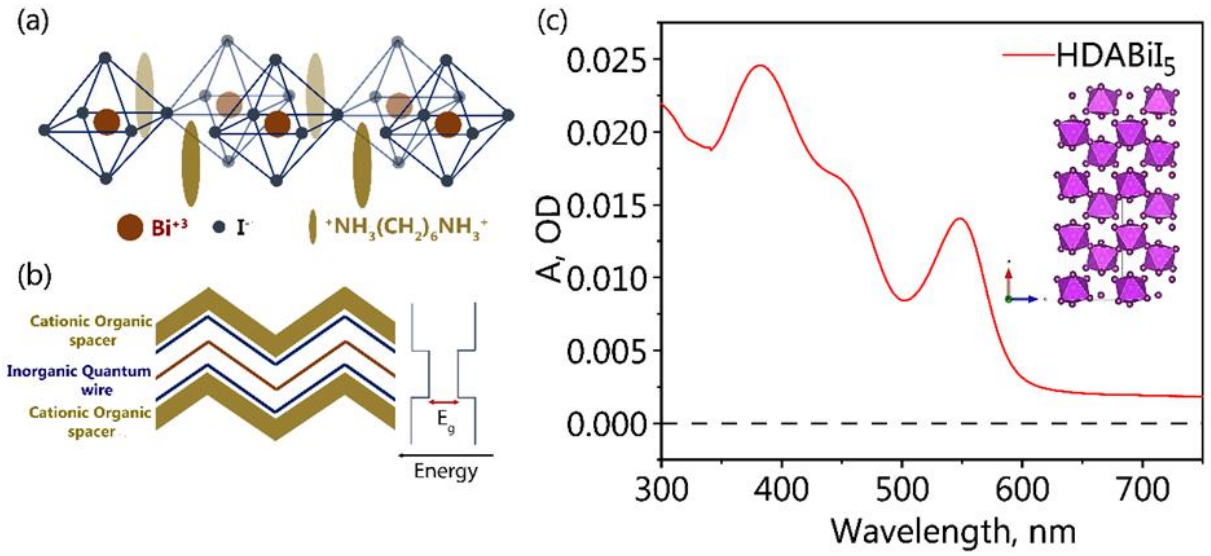

Figure 1 (a) Schematic of $HDABiI_5$ One-dimensional quantum wire; (b) Schematic representing bandgap in the quantum wire; (c) Steady-state absorption spectra of $HDABiI_5$ (Inset: the Bi-I framework from the single crystal structure)

perovskite structures are determined by the Goldschmidt tolerance factor. As the size of the organic cation increases, it pushes away the inorganic structure to form a lower dimensional motif. The organic cations act as spacers and stabilizers for these lower dimensional materials.

In terms of optical properties, the lower dimensional structures resemble well established quantum confined semiconductors, although there are slight differences. The traditional semiconductor quantum well is a rigid structure with low electron-phonon couplings. In the case of perovskites, the quantum wells are separated by organic cations that have vibrational and rotational degrees of freedom. Upon excitation, the change in electronic density in the inorganic layer is highly coupled with the lattice distortions in the structure[9–15]. Thus, excitation dynamics in perovskites is a complex interplay of quantum confinement effects and strong electron-phonon couplings. Another interesting aspect of perovskite is the band gap of the material, which is sensitive to the inorganic components; thus, the metal center and halide engineering can tune the bandgap very easily, keeping the geometry and connectivity the same.

With complexities such as non-rigid lattice and strong confinement effects, screening of excitons by surrounding lattice leads to the formation of coupled quasiparticles i.e., Exciton-Polarons[16,17]. These particles have been observed previously majorly in organic solids.[18,19] However, very recently, these excitations were observed for two-dimensional hybrid inorganic organic perovskites (2D-HOIPs) as primary excitations. These quasiparticles lead to the protection of excitons from non-linear scattering by dressing them up with surrounding lattice. Such screening can drive excitons into a self trapping bottleneck. Although these long and short range couplings have been assigned in 2D-HOIPs, there is no spectroscopic evidence for similar effects in one-dimensional analogs of HOIPs. A detailed understanding of the coupled modes in one-dimensional structure would allow for tweaking the exciton dynamics in such systems.

Here, we systematically studied the properties of excitons in quasi-1D corner-sharing Bismuth Iodide octahedra[20] (Figure 1a), which mimics 1D-perovskite structure using broadband transient absorption spectroscopy. With time dependent spectral traces, we evaluated spectral shifts, broadening, and dynamics of excitons in ultrafast timescales. Along with spectral features, we observed impulsively excited Raman coherences. From the Density functional theory (DFT) based electronic structure calculations, we assign these coherences to low frequency octahedral modes. These modes are the leading coordinate that derives the fast dynamics of excitons. We found the Electron-Phonon coupling constants, derived from amplitudes of the coherences, to be 10 times larger than that reported in 2D-perovskite materials. With our first foray of electron-phonon couplings in these special zig-zag quasi-1D structures, we envision that such materials will be used in newer optoelectronic devices along with other classes of quantum devices.

Results and Discussion

Figure 1(a) describes the structural characteristic of the **$HDABiI_5$** perovskite, where Bi^{+3} sits at the center of octahedral units coordinated with six iodide ions. These octahedral units are corner shared in a zigzag motif along a single axis. Such an arrangement of inorganic octahedra is stabilized by intercalated organic hexyl-diammonium cation $(NH_3CH_2)_6NH_3)^{+2}$. Organic cations either form Van der Waals interaction with chains of octahedra in Ruddlesden-Popper perovskites or dipolar/H-Bonding interactions in Dion-Jacobson perovskites, thereby stabilizing the lattice. Here, the stabilizing effects come from the H-bonding of ammonium N-H, with the iodide constituting the inorganic octahedra. The detailed crystal structure and lattice parameters are given in the supplementary file. The structure of such a lattice is represented in Figure 1(b), the organic layer has a much higher bandgap with respect to the inorganic layer. This is highly interesting as the organic layer has vacant orbitals much higher in energy to host a charge, thus any charge placed in the lattice only moves into the inorganic chain facing electronic confinement. Further, the organic chains have low dielectric constants i.e., the Coulombic interaction within the organic cation is stronger compared to the inorganic layers. Thus, the inorganic layer hosts much weaker binding energies for the excited states. Optical excitation for the inorganic layer Figure 1(c), can be divided into two regions - excitonic resonance at band-edge and excitations in higher excitonic features overlapped with continuum bands. Organic cations are comprised of alkyl chains and ammonium moieties absorbing in

deep UV thus excitations at the band edge are expected to be in inorganic confinement leading to strongly bound excitons i.e., stable Wannier like excitons at room temperature. From our electronic structure calculations, similar inferences can be drawn as the calculated density of states (DOS) shows a major

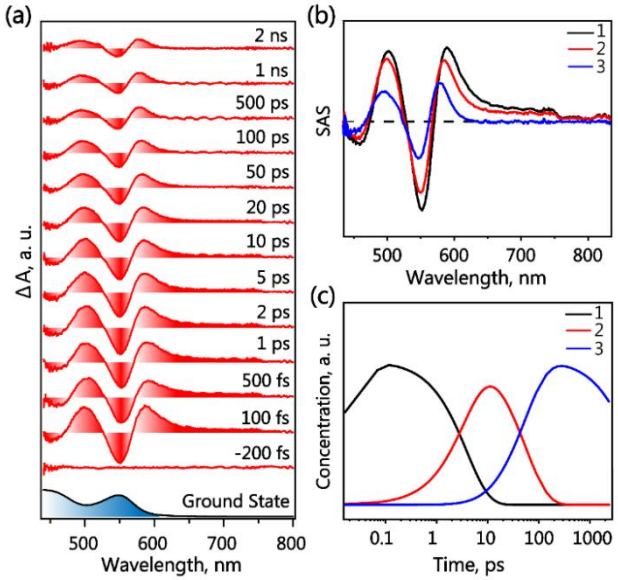

Figure 2. (a) Femtosecond transient absorption spectra of $HDABiI_5$ at 520 nm excitation at different time points; (b) Representative state decay spectra after singular value decomposition; (c) Representative kinetics for the corresponding states after Singular Value decomposition.

contribution at the band edge from the inorganic components Bi and I, while C, N, and H have contributions toward the UV region as shown in Supplementary Figure S15.

Figure 2 describes the transient absorption spectra for **$HDABiI_5$** after photoexcitation at 520 nm. Within 100 fs, a complex spectra was observed with ground state bleach and for every bleach feature, there is a corresponding red-shifted excited state resonance feature. To understand these resonance features, all possible transient absorption profiles for a lower dimensional material are well summarized in the supplementary Figure 10. This typical red-shifted excited state resonances had been assigned to bandgap renormalization where the bandgap of the material changes due to the presence of excitons. The dynamics of these excitons were extracted via singular value decomposition for all the spectral features. The components are shown in Figure 2(b) and (c), there are three decay components of 3.7 ps, 60 ps, and a non-decaying feature. There is a gradual blue shift in the excitonic resonances with increasing time. The gradual blue shift is a consequence of the dynamic screening of excitons into a trap state. Excitations at higher wavelengths 490 nm, and 400 nm exhibit similar spectral features, and the decay of the exciton matches well with the excitation at 520 nm (Figures S3 & S4). Excitations into higher lying excitons decay quickly into band edge excitonic states within IRF limited timescales. Nanosecond to microsecond measurements were performed to measure the lifetime of these long-lived excitonic states. The spectral features remained unchanged at the nanosecond timescale without any observed blue shift with a decrease in intensity over hundreds of nanoseconds (Figure S5 in SI). The excitonic features show a characteristic two-component decay in nanosecond timescales previously reported for self-trapped excitons[21,22]. The spectral features showed decay with 60 ns and 450 ns of timescales. Along with an excitonic absorption, there is a red-shifted broad resonance from 600 to 750 nm. These red-shifted resonances were short-lived lived up to 50 ps. In the spectra, more complexities can arise as the excitons can interact with the ions or with themselves in the lattice to form many body quasiparticles such as trions or biexcitons. These red-shifted broad resonances have been assigned to free carriers or complex quasiparticles present after photoexcitation and observed fast dynamics are characteristic of carrier quenching of these carriers at defect sites.

In Fig. 3, we show a more rigorous analysis of excitonic shifts and line widths. The excitonic parameters were extracted by fitting all the resonance features with Gaussian functions at each time point[23]. The detailed analytic scheme is well described in supplementary Figure S12. All fittings were performed in a restricted narrow window from 1.9 eV to 2.27 eV. This allows us to avoid the broad red-shifted feature from the fitted data, as it may mislead the fitting Gaussians. On fitting, there is a gradual blueshift in the excitonic feature, as shown in Fig 4(a). Linewidth of the excitonic feature remained the same with a slight narrowing from 55 meV to 49 meV. This narrowing results from exciton trapping into a local defect induced potential or increased electric fields in the material after photoexcitation. The Gaussian fitting approach gives us an idea that excitons were initially in a hot state, further dissipating energy, leading to a fast blue shift in a few picosecond timescales. This is analogous to the internal conversion of molecules where molecules dissipate energy to the bath via vibration degrees of freedom. At higher timescales, excitons interact with each other thus relaxation leading to blue shift gradually with $\tau \sim 100$ ps. We hypothesize, after sufficient dissipation, excitons trap to a local disorder in the one-dimensional chain of octahedra which is evident from the data as no significant spectral shift and linewidth broadening is observed in the spectra after 100 picoseconds of timescale. Such localization of excitations has been previously reported with 2D Ruddlesden Popper perovskites where excitons form “puddles” or localized states after a degree of blue shift[23]. This localization is a consequence of a highly disordered energy landscape of one-dimensional perovskite with numerous degrees of freedom.

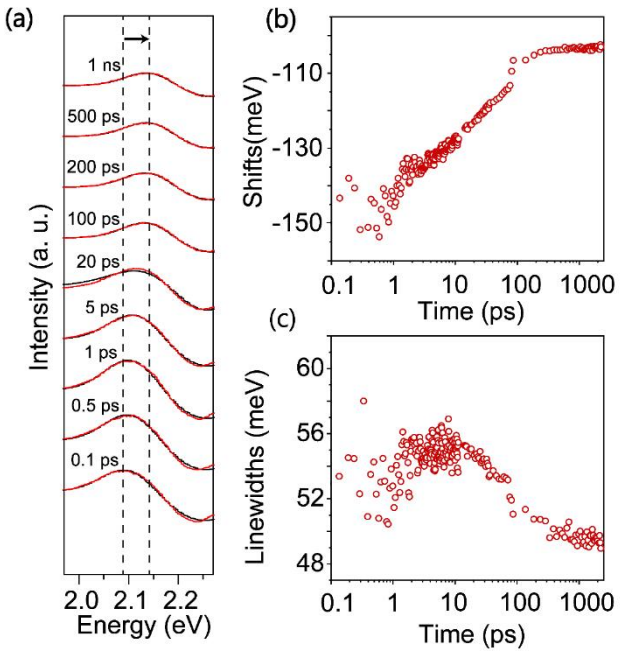

Figure 3. (a) Jacobian transforms stack plots of transient absorption fitted data with sum of Gaussians; (b) Excitonic shift vs time plot; (c) Excitonic linewidth vs Time plot.

In the initial time points of the transient absorption data shown in Figure 4 (a), there is clear observation of an oscillatory feature in the transient intensities of the excitonic absorption.

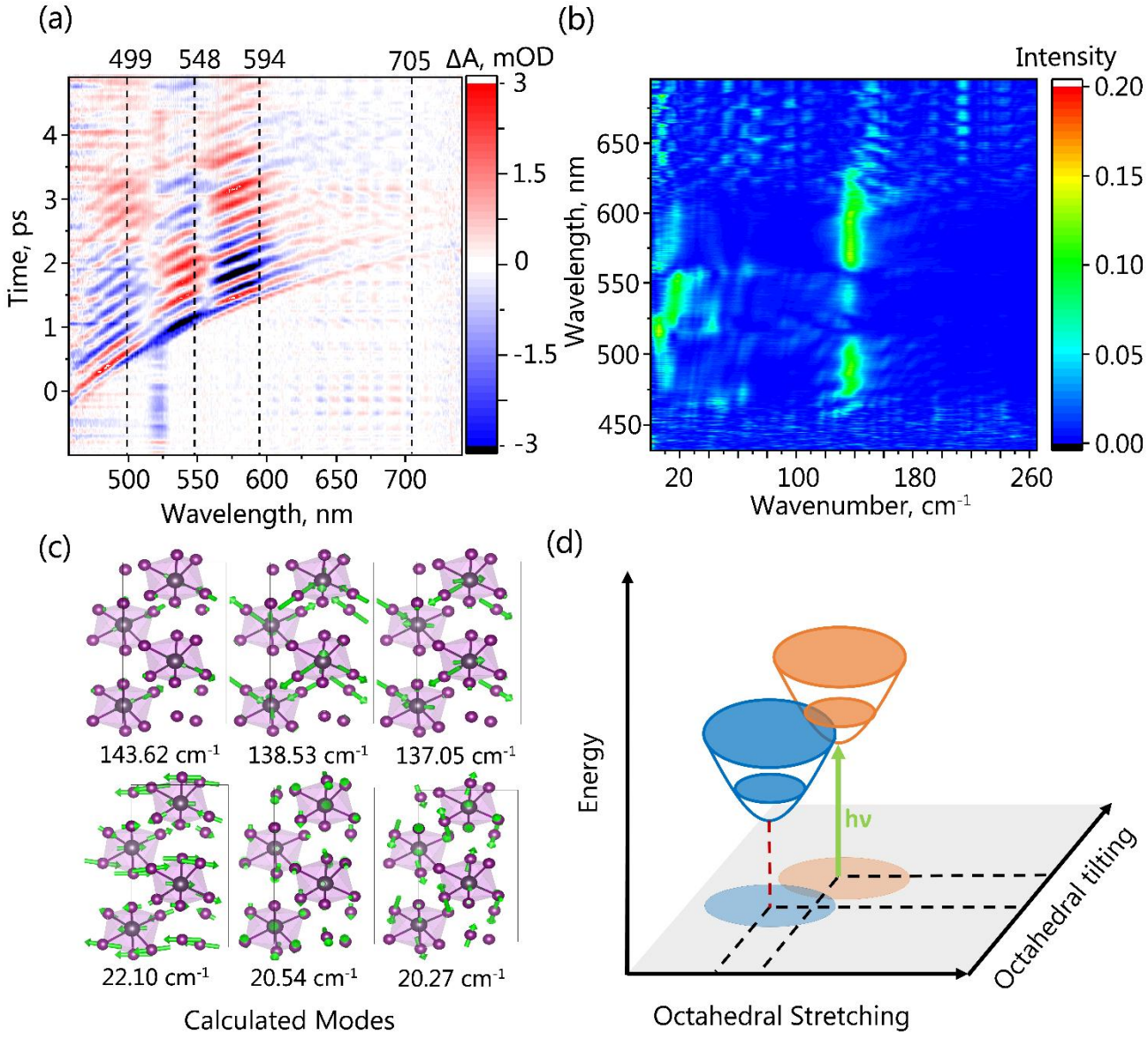

Figure. 4 (a) Residual contour plot after Global analysis; (b) Fourier transformed Raman profile for Impulsive excitation at 520 nm in $HDABiI_5$; (c) Calculated Modes for $HDABiI_5$; (d) Schematic representation of Exciton-Polaron in structurally displaced coordinate.

These oscillatory features can be assigned to optical phonon modes which have been impulsively excited by the broadband excitation of the femtosecond pulse. Strong electron-phonon coupling has been previously observed in Bismuth bromide double perovskites which indicates that our observations are convincing[24]. When plotting transient dynamics at different wavelengths indeed we observed phase changes in oscillations indicating that these are not arising from instrumental artifacts but are native to the excited state evolution. On excitation, these strong couplings can lead to coherent optical phonons. The basic mechanism of optical phonons generation is discussed in the supplementary figure S9. Since the oscillations are phase-shifted with respect to ground state features the mechanism is displacive excitation of coherent phonons (DECP). The Fourier transform of oscillations was performed at all the wavelengths as shown in Figure 4(b). At the ground state bleach feature, we observe a high-frequency mode at 140 cm^{-1} and a low-frequency lattice mode around 15 cm^{-1}. At the excited state absorption feature (590 nm), the intensity of the high-frequency mode is amplified i.e., becomes more prominent in the presence of excitons, and the low-frequency mode shifts to lower frequencies. The detailed pre-processing for clearly extracting the oscillation from the transient decay background is discussed in Figure S8. This indicates there is a structural relaxation in the presence of excitons. These oscillations were only observed for the excitonic features, the broad feature does not have any phonons coupled with it. These strong coupling and observation of low-frequency vibrations coupled to excitonic dynamics is direct evidence of the formation of "Exciton Polarons"[25–29].

Electronic Structure calculations

Density functional theory (DFT) based electronic structure calculations were performed to investigate the structural, electronic, and optical properties of HDA-BiI_5 crystal. Lattice parameters of the selected bulk form of HDA-BiI_5 crystal are a=13.95 Å, b=8.53 Å, and c=14.93 Å, respectively with a total of 128 atoms. The optimized structural configuration of HDA-BiI_5 is shown in Figure S13 while Bi, I, C, H, and N atoms are shown in Black, Red, brown, light pink, and blue color, respectively. To get insights into the structural bond variations upon optimization first we analyzed the pair correlation and radial distribution. As can be seen in Figure S14, Bi-I bond lengths are in the range of 2.94 Å – 3.26 Å. The calculated formation energy of HDA-BiI_5 is -

1.89 eV/atom indicating that the optimized structure of HDA-BiI5 is thermodynamically stable. The Partial Radial Distribution Function as shown in Figure S13 provides valuable insights into the spatial distribution of different atoms within a system. It measures the probability of finding an atom of a particular type at a specific distance from another atom of a designated type.

Modes (cm^{-1})	λ(meV)	S	D
140	15.90	0.9157	1.353
17	9.40	4.46	2.986

Table 1. Experimentally derived Electron phonon coupling parameters

This information is crucial for understanding the arrangement and ordering of specific pairs of atoms within the overall system. We observed sharp peaks in radial distribution indicated at selected pair correlation distance which is represented in Figure S13.

The calculated spin-polarized electronic band structure and the corresponding total density of states (DOS) and atom-projected DOS are depicted in Supplementary Figure S15. The band structure shows that HDA-BiI_5 is of an indirect band type with the corresponding valence band maximum (VBM) located at the half of the Γ-Z line near the Fermi vicinity. The conduction band minimum (CBM) of the unoccupied band is at Γ-point with the indirect (direct) band gap of 1.98 eV (2.01 eV). The determined band gap based on our calculations is comparable with the experimentally observed value of 1.89 eV. The projected DOS in the energy range from -4.0 eV to the Fermi level can be divided into two regions in the valence band regime. In the energy range from -4.00 eV to -2.00 eV, it originates mainly from the atoms of the organic part (HDA molecule), while from -2.00 eV to 0 eV, the valence band is dominated by the p orbitals of iodine atoms. The conduction band is mainly composed of the contribution of bismuth atoms, combined with some contribution from iodine atoms. Further, due to the presence of heavy elements like Bismuth, we have also calculated electronic band structure and the corresponding total density of states (DOS) and atom projected DOS considering spin-orbit coupling (SOC), and are given in Supplementary Figure S16. The band structure shows that HDA-BiI_5 is of an indirect band type. The valence band maximum (VBM) is located at the half of the Γ-Z line, which is close to the Fermi-energy level. The conduction band minimum (CBM) of the unoccupied band is in between B-Γ. We observed that with consideration of the SOC effect, the band gap is reduced to the indirect (direct) energy gap of 1.43 eV (1.46 eV). Similarly, the DOS in the energy range from -4.0 eV to the Fermi level can be divided into two regions. In the energy range from -4.00 eV to -2.00 eV, it originates mainly from the atoms of the organic part (HDA molecule). But, from -2.00 eV to 0 eV, the valence band is dominated by the p orbitals of iodine atoms. The conduction band is mainly composed of the contribution of bismuth atoms, combined with some contribution from iodine atoms.

We have additionally determined the force constants using density functional perturbation theory (DFPT) as implemented in Phonopy. The phonon band structure and phonon total density of states are depicted in Figure S17, where a large number of flat bands are arising due to the localized density of states in the system. There were a total of 384 modes, out of which 3 were imaginary. This is due to the noisy forces which arise while calculating force constants. The wave number of a total of 381 normal modes ranges from 20 cm^{-1} (lowest) to 3312.62 cm^{-1} (highest), while the configurations at the lowest three optical frequency phonon modes are displayed in Fig 4(c). The contribution of the inorganic component (BiI_5) is significant as compared to that of HDA molecules. Phonon DOS was sampled using an 11×11×11 Monkhorst-Pack k-point grid. In the smearing method, we used the Gaussian function for the corresponding delta function with the standard deviation specified by 0.1 sigma value.

Overall, the vibrational modes could be classified into three types: rocking, twisting, and wagging. Due to the complexity of lattice collective motion, we have shown only the contribution of BiI_5 for better representation. We observed mainly twisting and rocking modes at these three lowest frequencies. Further, we have also calculated the frequency-dependent dielectric properties of HDA-BiI_5. The real and imaginary parts of the dielectric function are shown in Supplementary Fig 18. The real part of the dielectric function reveals that the static dielectric constants along the x-, y-, and z-axis are 5.39, 5.55, and 5.07. The imaginary part of the dielectric function also reveals the anisotropic nature of the considered HDA-BiI_5 crystal. This can be observed from the position of the main absorption peaks among its components, which are slightly located at different energies.

Our density functional theory calculations reveal that HDA-BiI_5 is energetically stable with a formation energy of -1.89 eV. Electronic structure calculations reveal that the estimated indirect (direct) band gap is 1.43 (1.46 eV) and 1.98 (2.01 eV) with and without the inclusion of spin-orbit coupling. The phonon band structure and phonon DOS indicate the thermodynamic stability. Though we observed three imaginary acoustic modes at ambient pressure, it is worth noting that the imaginary phonon frequencies will disappear at elevated temperatures and pressure due to lattice anharmonicity. To estimate the strength of coupling from the observed oscillatory artifacts in transient absorption, we calculate reorganization energy from the model based on excitations in a displacive harmonic potential[10,11,30,31]. This model expresses the oscillation amplitude as $A_{OSC} = \frac{dOD}{dE} . \lambda$, where A_{OSC} is amplitude of oscillations, $\frac{dOD}{dE}$ is numerically calculated from steady state absorption spectra (both A_{OSC}, $\frac{dOD}{dE}$ are normalized with respect to excitation frequency), λ is reorganization energy. Further, λ can be expressed in terms of Huang Rhys factor S as $S = \frac{d^2}{2}$, giving a measure of coupling strength independent of mode energies i.e., the number of phonons dissipated for a mode; and d is a dimensionless quantity representing the lattice displacement from the normal coordinates. All the calculated parameters are tabulated in Table 1. For comparison, the derived parameters are much larger compared to a bulk inorganic lattice (S<0.05) and are an order of magnitude larger than the 2D perovskites reported till now (S=0.11-0.3)[28,32]. This suggests that much larger lattice distortion happens in the presence of excitons than in 2D halide perovskites.

Conclusion

In summary, here we provide a detailed dynamic picture of the nature of excitons in quasi one-dimensional lattice of $HDABiI_5$. After photoexcitation, excitons are long-lived up to 400 ns indicating the formation of “exciton polarons”. The exciton polaron arises due to the dressing with low-frequency phonon modes centered at BiI_6^{3-} octahedra. The observed changes in the transient absorption spectra especially the intensities and the linewidth indicate the dressing, and subsequently excitons interact strongly, and gradually these interactions fall away. The gradual blue shift observed corresponds to the cooling of these excitons in the perovskite lattice. The gradual cooling is a consequence of excitons scattering with itself in the one-dimensional lattice and further getting self-trapped at longer time scales forming excitonic puddles along the axis of inorganic chains. We envision that motivated by our work on corner-sharing 1D-chains of BiI_5 octahedra, the community will explore the chemical space of inorganic substitutions to drive modular exciton-polaron formation with seamless evolution to either long-lived trapped

charges or long-range exciton transport for numerous applications in optoelectronics and catalysis.

Supporting Information

The authors have attached a supporting information document along with the main text.

Acknowledgements

D.K.T and J.D. acknowledge support from the Department of Atomic Energy (DAE), Government of India, under Project No. 12-RandD-TFR-5.10-0100. SSD and SC would like to acknowledge the supercomputing facility of HRI. PKN acknowledges support from the Department of Atomic Energy (DAE), Government of India, under Project No. RTI 4007, and the Department of Science and Technology under the Swarna Jayanti fellowship

Keywords: Exciton-Polaron, Impulsive Raman spectroscopy, low dimensional perovskite, exciton dynamics.

(1) Mueller, T.; Malic, E. Exciton Physics and Device Application of Two-Dimensional Transition Metal Dichalcogenide Semiconductors. *npj 2D Mater. Appl.* **2018**, *2* (1), 29. https://doi.org/10.1038/s41699-018-0074-2.

(2) Scholes, G. D.; Rumbles, G. Excitons in Nanoscale Systems. *Nat. Mater.* **2006**, *5* (9), 683–696. https://doi.org/10.1038/nmat1710.

(3) High, A. A.; Hammack, A. T.; Butov, L. V; Hanson, M.; Gossard, A. C. Exciton Optoelectronic Transistor. *Opt. Lett.* **2007**, *32* (17), 2466–2468. https://doi.org/10.1364/OL.32.002466.

(4) Xiao, J.; Zhao, M.; Wang, Y.; Zhang, X. Excitons in Atomically Thin 2D Semiconductors and Their Applications. **2017**, *6* (6), 1309–1328. https://doi.org/doi:10.1515/nanoph-2016-0160.

(5) Schindler, C.; Zimmermann, R. Analysis of the Exciton-Exciton Interaction in Semiconductor Quantum Wells. *Phys. Rev. B* **2008**, *78* (4), 45313. https://doi.org/10.1103/PhysRevB.78.045313.

(6) Fu, J.; Xu, Q.; Han, G.; Wu, B.; Huan, C. H. A.; Leek, M. L.; Sum, T. C. Hot Carrier Cooling Mechanisms in Halide Perovskites. *Nat. Commun.* **2017**, *8* (1), 1300. https://doi.org/10.1038/s41467-017-01360-3.

(7) Yan, Y. J.; Mukamel, S. Femtosecond Pump-Probe Spectroscopy of Polyatomic Molecules in Condensed Phases. *Phys. Rev. A* **1990**, *41* (11), 6485–6504. https://doi.org/10.1103/PhysRevA.41.6485.

(8) Tran, N. L.; Elkins, M. H.; McMeekin, D. P.; Snaith, H. J.; Scholes, G. D. Observation of Charge Generation via Photoinduced Stark Effect in Mixed-Cation Lead Bromide Perovskite Thin Films. *J. Phys. Chem. Lett.* **2020**, *11* (23), 10081–10087. https://doi.org/10.1021/acs.jpclett.0c03044.

(9) Nie, Z.; Gao, X.; Ren, Y.; Xia, S.; Wang, Y.; Shi, Y.; Zhao, J.; Wang, Y. Harnessing Hot Phonon Bottleneck in Metal Halide Perovskite Nanocrystals via Interfacial Electron–Phonon Coupling. *Nano Lett.* **2020**, *20* (6), 4610–4617. https://doi.org/10.1021/acs.nanolett.0c01452.

(10) Ghosh, T.; Aharon, S.; Etgar, L.; Ruhman, S. Free Carrier Emergence and Onset of Electron–Phonon Coupling in Methylammonium Lead Halide Perovskite Films. *J. Am. Chem. Soc.* **2017**, *139* (50), 18262–18270. https://doi.org/10.1021/jacs.7b09508.

(11) Sagar, D. M.; Cooney, R. R.; Sewall, S. L.; Dias, E. A.; Barsan, M. M.; Butler, I. S.; Kambhampati, P. Size Dependent, State-Resolved Studies of Exciton-Phonon Couplings in Strongly Confined Semiconductor Quantum Dots. *Phys. Rev. B* **2008**, *77* (23), 235321. https://doi.org/10.1103/PhysRevB.77.235321.

(12) Yang, Y.; Ostrowski, D. P.; France, R. M.; Zhu, K.; van de Lagemaat, J.; Luther, J. M.; Beard, M. C. Observation of a Hot-Phonon Bottleneck in Lead-Iodide Perovskites. *Nat. Photonics* **2016**, *10* (1), 53–59. https://doi.org/10.1038/nphoton.2015.213.

(13) Wright, A. D.; Verdi, C.; Milot, R. L.; Eperon, G. E.; Pérez-Osorio, M. A.; Snaith, H. J.; Giustino, F.; Johnston, M. B.; Herz, L. M. Electron–Phonon Coupling in Hybrid Lead Halide Perovskites. *Nat. Commun.* **2016**, *7* (1), 11755. https://doi.org/10.1038/ncomms11755.

(14) Ni, L.; Huynh, U.; Cheminal, A.; Thomas, T. H.; Shivanna, R.; Hinrichsen, T. F.; Ahmad, S.; Sadhanala, A.; Rao, A. Real-Time Observation of Exciton–Phonon Coupling Dynamics in Self-Assembled Hybrid Perovskite Quantum Wells. *ACS Nano* **2017**, *11* (11), 10834–10843. https://doi.org/10.1021/acsnano.7b03984.

(15) Mayers, M. Z.; Tan, L. Z.; Egger, D. A.; Rappe, A. M.; Reichman, D. R. How Lattice and Charge Fluctuations Control Carrier Dynamics in Halide Perovskites. *Nano Lett.* **2018**, *18* (12), 8041–8046. https://doi.org/10.1021/acs.nanolett.8b04276.

(16) Dai, Z.; Lian, C.; Lafuente-Bartolome, J.; Giustino, F. Theory of Excitonic Polarons: From Models to First-Principles Calculations. *Phys. Rev. B* **2024**, *109* (4), 45202. https://doi.org/10.1103/PhysRevB.109.045202.

(17) Biswas, S.; Alowa, F.; Zhao, R.; Zacharias, M.; Sharifzadeh, S.; Coker, D. F.; Seferos, D. S.; Scholes, G. D. Exciton-Phonon Coupling Controls Exciton-Polaron Formation and Hot Carrier Relaxation in Rigid Dion-Jacobson Type Two-Dimensional Perovskites; **2023** arXiv:2305.01741v1**.**

(18) Liu, E.; van Baren, J.; Lu, Z.; Taniguchi, T.; Watanabe, K.; Smirnov, D.; Chang, Y.-C.; Lui, C. H. Exciton-Polaron Rydberg States in Monolayer MoSe2 and WSe2. *Nat. Commun.* **2021**, *12* (1), 6131. https://doi.org/10.1038/s41467-021-26304-w.

(19) Dai, Z.; Lian, C.; Lafuente-Bartolome, J.; Giustino, F. Excitonic Polarons and Self-Trapped Excitons from First-Principles Exciton-Phonon Couplings. *Phys. Rev. Lett.* **2024**, *132* (3), 36902. https://doi.org/10.1103/PhysRevLett.132.036902.

(20) Mousdis, G. A.; Papavassiliou, G. C.; Terzis, A.; Raptopoulou, C. P. No Title. *Zeitschrift für Naturforsch. B* **1998**, *53* (8), 927–932. https://doi.org/doi:10.1515/znb-1998-0825.

(21) Cortecchia, D.; Yin, J.; Bruno, A.; Lo, S.-Z. A.; Gurzadyan, G. G.; Mhaisalkar, S.; Brédas, J.-L.; Soci, C. Polaron Self-Localization in White-Light Emitting Hybrid Perovskites. *J. Mater. Chem. C* **2017**, *5* (11), 2771–2780. https://doi.org/10.1039/C7TC00366H.

(22) Yangui, A.; Garrot, D.; Lauret, J. S.; Lusson, A.; Bouchez, G.; Deleporte, E.; Pillet, S.; Bendeif, E. E.; Castro, M.; Triki, S.; Abid, Y.; Boukheddaden, K. Optical Investigation of Broadband White-Light Emission in Self-Assembled Organic–Inorganic Perovskite (C6H11NH3)2PbBr4. *J. Phys. Chem. C* **2015**, *119* (41), 23638–23647. https://doi.org/10.1021/acs.jpcc.5b06211.

(23) Wu, X.; Trinh, M. T.; Zhu, X. Excitonic Many-Body Interactions in Two-Dimensional Lead Iodide Perovskite Quantum Wells. *J. Phys. Chem. C* **2015**, *119*, 150311180828003. https://doi.org/10.1021/acs.jpcc.5b00148.

(24) Kentsch, R.; Scholz, M.; Horn, J.; Schlettwein, D.; Oum, K.; Lenzer, T. Exciton Dynamics and Electron–Phonon Coupling Affect the Photovoltaic Performance of the Cs2AgBiBr6 Double Perovskite. *J. Phys. Chem. C* **2018**, *122* (45), 25940–25947. https://doi.org/10.1021/acs.jpcc.8b09911.

(25) Srimath Kandada, A. R.; Silva, C. Exciton Polarons in Two-Dimensional Hybrid Metal-Halide Perovskites. *J. Phys. Chem. Lett.* **2020**, *11* (9), 3173–3184. https://doi.org/10.1021/acs.jpclett.9b02342.

(26) Thouin, F.; Valverde-Chávez, D. A.; Quarti, C.; Cortecchia, D.; Bargigia, I.; Beljonne, D.; Petrozza, A.; Silva, C.; Srimath Kandada, A. R. Phonon Coherences Reveal the Polaronic Character of Excitons in Two-Dimensional Lead Halide Perovskites. *Nat. Mater.* **2019**, *18* (4), 349–356. https://doi.org/10.1038/s41563-018-0262-7.

(27) Seiler, H.; Zahn, D.; Taylor, V. C. A.; Bodnarchuk, M. I.; Windsor, Y. W.; Kovalenko, M. V; Ernstorfer, R. Direct Observation of Ultrafast Lattice Distortions during Exciton–Polaron Formation in Lead Halide Perovskite Nanocrystals. *ACS Nano* **2023**, *17* (3), 1979–1988. https://doi.org/10.1021/acsnano.2c06727.

(28) Hurtado Parra, S.; Straus, D. B.; Fichera, B. T.; Iotov, N.; Kagan, C. R.; Kikkawa, J. M. Large Exciton Polaron Formation in 2D Hybrid Perovskites via Time-Resolved Photoluminescence. *ACS Nano* **2022**, *16* (12), 21259–21265. https://doi.org/10.1021/acsnano.2c09256.

(29) Cannelli, O.; Colonna, N.; Puppin, M.; Rossi, T. C.; Kinschel, D.; Leroy, L. M. D.; Löffler, J.; Budarz, J. M.; March, A. M.; Doumy,

G.; Al Haddad, A.; Tu, M.-F.; Kumagai, Y.; Walko, D.; Smolentsev, G.; Krieg, F.; Boehme, S. C.; Kovalenko, M. V; Chergui, M.; Mancini, G. F. Quantifying Photoinduced Polaronic Distortions in Inorganic Lead Halide Perovskite Nanocrystals. *J. Am. Chem. Soc.* **2021**, *143* (24), 9048–9059. https://doi.org/10.1021/jacs.1c02403.

(30) Zacharias, M.; Giustino, F. Theory of the Special Displacement Method for Electronic Structure Calculations at Finite Temperature. *Phys. Rev. Res.* **2020**, *2* (1), 13357. https://doi.org/10.1103/PhysRevResearch.2.013357.

(31) Fu, J.; Li, M.; Solanki, A.; Xu, Q.; Lekina, Y.; Ramesh, S.; Shen, Z. X.; Sum, T. C. Electronic States Modulation by Coherent Optical Phonons in 2D Halide Perovskites. *Adv. Mater.* **2021**, *33* (11), 2006233. https://doi.org/https://doi.org/10.1002/adma.202006233.

(32) Zhang, H.; Li, W.; Essman, J.; Quarti, C.; Metcalf, I.; Chiang, W.-Y.; Sidhik, S.; Hou, J.; Fehr, A.; Attar, A.; Lin, M.-F.; Britz, A.; Shen, X.; Link, S.; Wang, X.; Bergmann, U.; Kanatzidis, M. G.; Katan, C.; Even, J.; Blancon, J.-C.; Mohite, A. D. Ultrafast Relaxation of Lattice Distortion in Two-Dimensional Perovskites. *Nat. Phys.* **2023**, *19* (4), 545–550. https://doi.org/10.1038/s41567-022-01903-6.

Table of Contents